An ab initio study of the electronic properties of the ferroelectric heterostructure In2Se3/Bi2Se3

Tarek Ayadi, Lamjed Debbichi, M Said, Dario Rocca, Sébastien Lebègue

Version of Record: https://www.sciencedirect.com/science/article/pii/S0169433220328233
Manuscript_c63ce00af4e0be9ddb34c3e685092a5e

An ab initio study of the electronic properties of the ferroelectric heterostructure In_2Se_3/Bi_2Se_3

T. Ayadi,[1,2,*] L. Debbichi,[2] M. Badawi,[2] M. Said,[1] D. Rocca,[2] and S. Lebègue[2]

[1] *Laboratoire de la Matière Condensée et des Nanosciences, Faculté des Sciences, Université de Monastir, 5019 Monastir, Tunisia .*

[2] *Laboratoire Physique et Chimie Théoriques (LPCT, UMR CNRS UL 7019), Institut Jean Barriol, Université de Lorraine, BP 239, Boulevard des Aiguillettes, 54506 Vandoeuvre-lès-Nancy, Cedex, France*

Abstract

Using ab initio calculations, we have investigated the electronic properties of the bidimensional ferroelectric heterostructure In_2Se_3/Bi_2Se_3. Depending on the direction of the polarization vector of the In_2Se_3 layer, we found that the In_2Se_3/Bi_2Se_3 heterostructure can have either a direct or an indirect bandgap, with values of 0.67 or 1.00 eV obtained with the GW approximation. Also this material presents a type II band alignment and appears to be a promising system for electron-hole separation. Finally, we found that an external electric field can be used to control not only the electronic gap but also the band offsets and the type of band alignment, which is very promising for certain applications in electronic and optoelectronic.

* tarek.ayadi91@yahoo.fr

I. INTRODUCTION

The increasing progress of nanotechnology in recent years has motivated the scientific community to study materials with improved or even new properties, including two-dimensional (2D) materials[1–7]. The latter, in the form of nanometric objects, have already demonstrated their effectiveness as active elements in various devices capable to meet the current needs. In particular, 2D piezoelectricity and 2D ferroelectricity[8–10] have attracted tremendous attention due to their large potential for device applications. These properties are exploited for applications as nonvolatile ferroelectric memories[11], capacitors[12], actuators[13], and sensors[14].

The ability to combine and stack 2D layers has created a new class of materials known as van der Waals heterostructures and has opened the way to design new architectures. This area has already proven to be fruitful for new properties and various functionalities, different from those of their individual 2D materials and thus created the basis for a variety of devices[15, 16]. For instance, Zhang et *al* [17] have demonstrated that the photoresponsivity of a photodetector based on graphene/MoS_2 heterostructures is improved by a factor of nine in comparison with a standalone graphene layer. Also, enriching the functionalities of 2D heterostructures with ferroelectric properties would open up new opportunities for their applications [18–20].

Obviously the properties of this type of heterostructures are directly linked to the properties of their elementary constituents. Recently, both experiment and theoretical studies[21–23] on In_2Se_3 proved that the α phase presents ferroelectric properties with in- and out-of plane polarization, contrary to the β phase which is not ferroelectric. This discovery puts α-In_2Se_3 under the light to be a useful candidate to form 2D ferroelectric heterostructures with out of plane polarization[24, 25]. For example, theoretical studies[23, 26] demonstrated that the In_2Se_3/graphene heterostructure exhibits a Schottky barrier which can be controlled by the direction of the out-of plane intrinsic dipole of α-In_2Se_3. Moreover, a photodetector with outstanding properties, including a photocurrent on/off ratio of 1.24 x 10^5 at room temperature and a maximum photoresponsivity of 26 mAW^{-1} at 650 nm, based on WSe_2/α-In_2Se_3 was fabricated recently[27]. On the other hand, the topological insulator Bi_2Se_3[28–31] is a good material to form van der Waals heterostructures with various promising applications: for instance, a high performance photodetector based on SnTe/Bi_2Se_3 was fabricated which

exhibits remarkable properties as a high light responsivity of 145.74 mAW^{-1} and a maximum detectivity of 1.15x10^{10} Jones[32]. At the limit of the single layer, Bi_2Se_3 possesses also great carrier mobilities of electrons and holes which can reach 1.96x10^5 and 3.4x10^4 $cm^2V^{-1}s^{-1}$, respectively, together with a high optical absorption in the near ultraviolet and visible light regions [33]. In addition, Somilkumar *et al* [34] have used molecular beam epitaxy (MBE) to grow Bi_2Se_3/In_2Se_3 bilayers on Si(111) and they found that In_2Se_3 is suitable for the subsequent high-quality heteroepitaxy of Bi_2Se_3. However, to our knowledge, no theoretical work has studied the electronic properties of the In_2Se_3/Bi_2Se_3 heterostructure and more specifically their band offsets.

In this work, DFT calculations were performed to investigate the electronic properties of the ferroelectric α-In_2Se_3/Bi_2Se_3 and the non-ferroelectric β-In_2Se_3/Bi_2Se_3 heterostructures. Moreover, we also have investigated their band offsets under electrical field which are important quantities for material and device designs.

II. COMPUTATIONAL DETAILS

Our first principles calculations based on density functional theory were performed using the Vienna Ab Initio Simulation Package (VASP)[35] implementing the projector augmented wave method [36]. The exchange and correlation potential was described by the Perdew-Burke-Ernzerhof functional within the generalized gradient approximation[37]. The weak van der Waals interactions are described by the dispersion correction of Tkatchenko and Scheffler[38] with iterative Hirshfeld partitioning[39] (TS/HI) as implemented [40, 41] in VASP. A 12x12x1 k-mesh was used for the Brillouin zone sampling and the cutoff energy was set to 500 eV. A vacuum of 17 Å along the direction perpendicular to the layers was adopted to ensure decoupling between periodically repeated systems. The convergence parameters were set to 0.01 eV/Å for the residual forces on ions and to 10^{-6} eV for the total energy. Since DFT in the generalized gradient approximation generally underestimates bandgaps, we have used the GW approximation [42, 43] to obtain realistic bandstructures. The cut-off for the polarizability matrices was set to 150 eV, while the other parameters (k-points, plane wave cut-off) were kept as in the DFT calculations.

III. RESULTS AND DISCUSSION

When stacking a Bi_2Se_3 layer on top of a α-In_2Se_3 ferroelectric layer, two different arrangements can be obtained, noted hereafter G_1 and G_2, depending on the direction of the polarization vector: in the G_1 configuration, the spontaneous out-of-plane electric polarization P is pointing towards Bi_2Se_3 while in the configuration G_2 it is pointing in the other direction. The G_3 configuration is constructed by stacking the Bi_2Se_3 layer on top of the non-ferroelectric layer β-In_2Se_3. The different geometries are shown in figure 1.

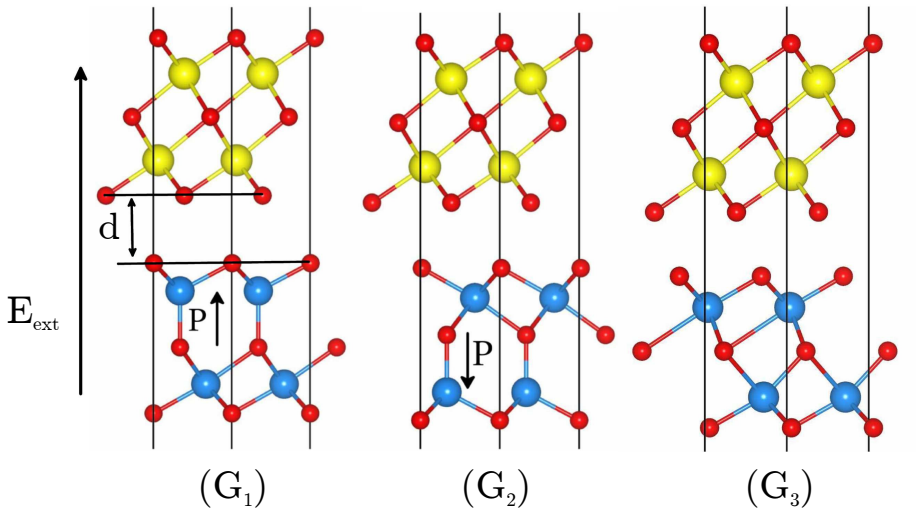

FIG. 1: Side view of the different configurations of the heterostructure In_2Se_3/Bi_2Se_3. The red spheres represent the selenium atoms, while the blue and yellow spheres correspond to indium and bismuth atoms, respectively. The black arrows indicate the direction of the spontaneous electric polarization (P). An electric field (E_{ext}) is applied perpendicularly to the layers.

The list of the different configurations of the In_2Se_3/Bi_2Se_3 heterostructure, their structural parameters, the interlayer binding energy and their calculated bandgap with different approximations are presented in table I. As expected, our optimized in-plane lattice parameter with the TS/HI method gives values ranging between the values of the isolated layers: the value for the G_1 and G_2 ferroelectric configurations is 4.10 Å, and it is 4.06 Å for the G_3 non-ferroelectric configuration, while the corresponding value for the isolated layers Bi_2Se_3, α-In_2Se_3 and β-In_2Se_3 is 4.15, 4.06 and 3.97 Å, respectively.

Also, we have calculated the interlayer distance (d) which corresponds to the selenium-

selenium distance along the stacking direction as presented in figure 1. To find the equilibrium interlayer distance, we have calculated the binding curve between the In_2Se_3 and Bi_2Se_3 layers. The binding energy per atom (defined as E_b= (E_0 - E_s)/N) between the In_2Se_3 and Bi_2Se_3 corresponds to the energy difference between the energy at equilibrium (E_0) and the energy when the layers are put at a distance large enough to avoid interlayer interactions (E_s), divided by the number of atoms in the cell (N). These calculated values are found to be in the same range as for other van der Waals heterostructures [44, 45], confirming the weak interaction between the layers.

TABLE I: Calculated interlayer distance d (Å), binding energy E_b (meV/atom), DFT (with and without spin-orbit coupling), and GW bandgaps of the different configurations of the heterostructure In_2Se_3/Bi_2Se_3.

	a (Å)	d (Å)	E_b (meV)	E_g (eV)		
				PBE	PBE+SOC	GW+SOC
G_1	4.10	2.92	19.70	0.37 (ΓM→Γ)	0.07 (Γ→Γ)	0.67
G_2	4.10	3.06	17.00	0.54 (ΓK→Γ)	0.38 (ΓK→Γ)	1.00
G_3	4.06	2.74	20.50	0.16 (ΓM→ M)	0.10 (ΓM→ M)	0.54

Then we have used the PBE and GW approximations to calculate the band structure (see figure 2) and the bandgap for all configurations. With PBE, we found that the valence band maximum (VBM) is along the ΓM direction for the G_1 and G_3 configurations and is along ΓK for the G_2 configuration. Also, we found that the conduction band minimum (CBM) is at the Γ point for both ferroelectric configurations (G_1 and G_2), and is at the M point for the non-ferroelectric configuration G_3.

When the spin-orbit coupling (SOC) is taken into account, the states of the VBM at the Γ point of the G_1 configuration, are shifted up and the CBM is shifted down in energy. The bandgap is now direct, with a reduction of about 0.3 eV. This value is increased to 0.67 eV when the GW approximation is used. However, when the intrinsic dipole of In_2Se_3 is in the opposite direction (the G_2 configuration), the SOC does not change the nature of the bandgap, but a reduction of the gap value of about 0.16 eV is observed. The SOC

decreases the electronic gap value up to 0.8 eV with PBE+SOC, but GW+SOC brings it up to 1 eV. For the configuration G_3, when the SOC is included, we found that there is a small energy variation (of a few meV) at the VBM and CBM levels. The gap is indirect of the order of 0.1 eV with PBE+SOC and the value increases up to 0.54 eV with GW+SOC. Generally, we observed that there are no major quantitative differences in the dispersion of bands found with GW+SOC compared to those found with PBE+SOC, the main difference being a wideing of the bandgap, as expected with the GW approximation. Due to the important effect of spin-orbit coupling on the electronic structures of the heterostructure In_2Se_3/Bi_2Se_3, it will be kept in the rest of our calculations.

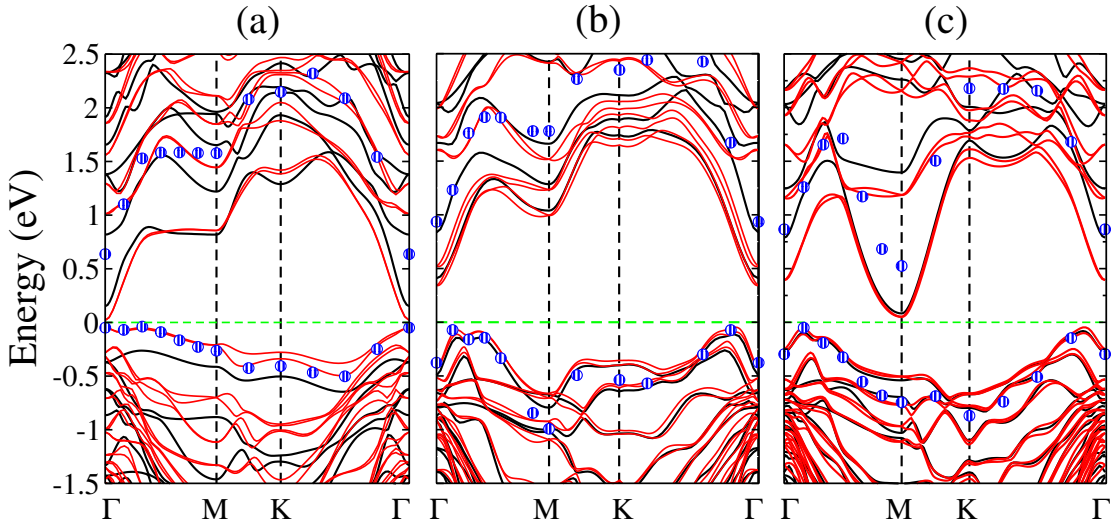

FIG. 2: Band structure of the (a) G_1, (b) G_2 and (c) G_3 configurations of In_2Se_3/Bi_2Se_3 heterostrcuture. The black and red lines represent the PBE and PBE+SOC calculations. The GW+SOC calculations for the last valence band and the first conduction band are shown with blue circles. The Fermi level is set to 0 eV.

To give a qualitative explanation of the nature of the VBM and CBM states, we have calculated, with PBE+SOC, the band structures with a projection on the orbitals of each layer, as presented in figure 3. For the G_1 configuration, where the intrinsic dipole is directed towards Bi_2Se_3, we found that the VBM states correspond mainly to the orbitals of the In_2Se_3 layer, while the CBM states are formed by the orbitals of the Bi_2Se_3 layer. By reversing the polarization of In_2Se_3 (the G2 configuration), the nature of the VBM and CBM states is reversed: we found that the VBM states are mainly contributed by the orbitals of Bi_2Se_3 while the CBM states are dominated by the orbitals of In_2Se_3, with a

small contribution of the orbitals of Bi_2Se_3. For the non-ferroelectric configuration G_3, we found that the VBM and CBM states are dominated by the orbitals of Bi_2Se_3 and In_2Se_3, respectively. These observations are consistent with a type II band alignment between In_2Se_3 and Bi_2Se_3, obtained by aligning the band energies of the single layer In_2Se_3 and Bi_2Se_3 in the heterostructure In_2Se_3/Bi_2Se_3 with respect to the vacuum level, as shown schematically in figure 3(d).

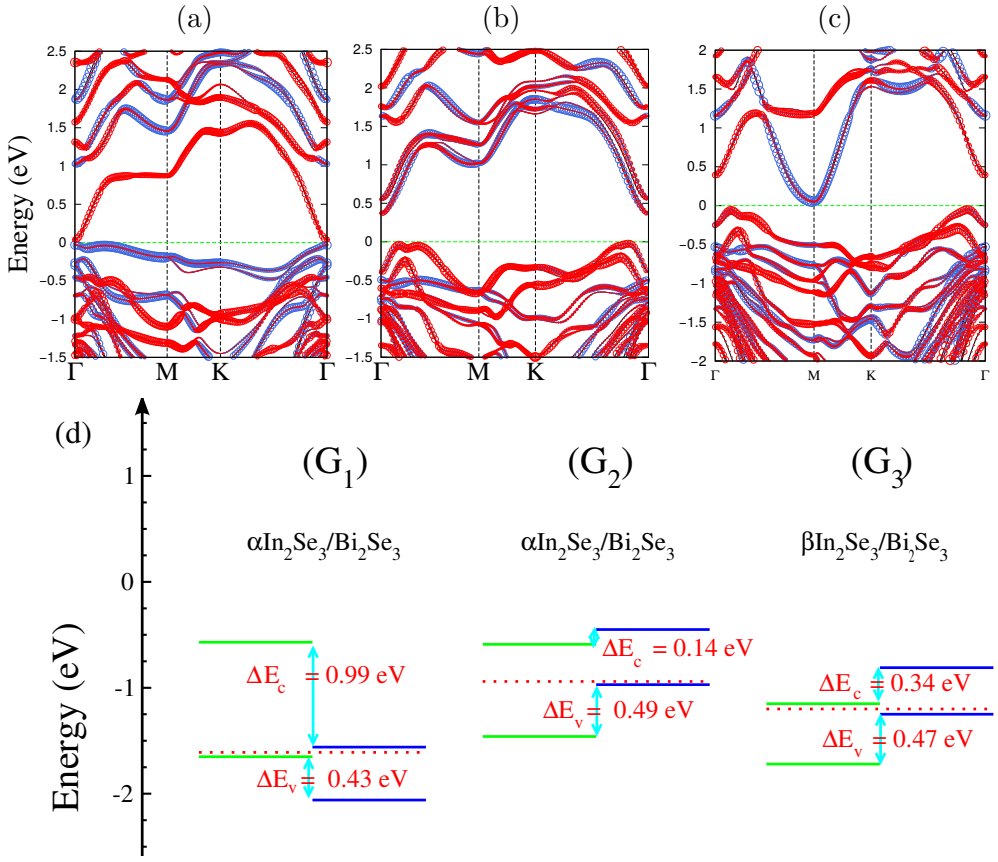

FIG. 3: PBE+SOC band structures of (a) G_1, (b) G_2 and (c) G_3 configurations of the In_2Se_3/Bi_2Se_3 heterostructure. The size of the blue and red circles is proportional to the In_2Se_3 and Bi_2Se_3 contributions, respectively. The Fermi level is set to 0 eV. (d) Band alignments of the different configurations of the heterostructure In_2Se_3/Bi_2Se_3. The relevant electronic parameters ($|\Delta E_c|$ and $|\Delta E_v|$) are also given in the figure. The red dashed lines are the different Fermi level.

To briefly examine the contribution of In_2Se_3 and Bi_2Se_3 layers in VBM and CBM, we present in figure 4 our calculated charge density corresponding to the top of the valence states

and the bottom of the conduction states. We observe in figure 4(a), which corresponds to the G_1 configuration, that the electrons and holes are separated and distributed on the layers Bi_2Se_3 and In_2Se_3, respectively. In the case of the G_2 configuration, we can clearly observe in figure 4(b) that the charge density at CBM states is found to be localized on In_2Se_3 while the VBM states belong to the Bi_2Se_3 layer. In figure 4(c), which corresponds to the non-ferroelectric configuration G_3, we found that the charge density at the VBM is localized mainly on Bi_2Se_3, while the charge density at the CBM is localized mainly on In_2Se_3. These observations are consistent with type II band alignment mentioned above, which make these configurations of the heterostructure suitable for an efficient electron-hole separation.

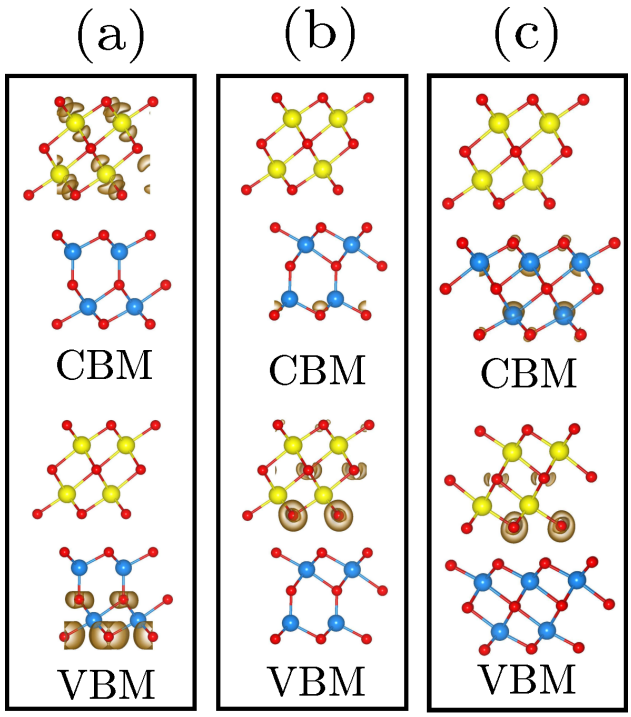

FIG. 4: The band-decomposed charge density of the CBM and VBM of the (a) G_1, (b) G_2 and (c) G_3 configurations of the In_2Se_3/Bi_2Se_3 heterostructure. The isosurface is chosen as $0.0015e^-/Å^3$.

We turn now to explore the effect of an external electric field E_{ext} on the electronic structure of the heterostructure In_2Se_3/Bi_2Se_3 using the PBE functional. The electric field is used here to simulate the presence of a gate voltage on the heterostructure, if used in a device. The positive sign of the external electric field E_{ext} is defined as shown in Figure 1. The evolution of the electronic bandgap of In_2Se_3/Bi_2Se_3 as a function of the external electric field E_{ext} is presented in Figure 5. It is seen that the heterostructure In_2Se_3/Bi_2Se_3

shows a significant modulation of its electronic gap by E_{ext}. For the G_1 configuration, where the intrinsic dipole P is pointing towards Bi_2Se_3, the variation of the band gap under the application of an external electric field is divided into three regions. In the first region, where the external electric field is between -0.8 and -0.5 V/Å, the gap value tends to be stable and the heterostructure achieves its maximum electronic gap with a value of about 0.51 eV. In the second region, where E_{ext} is between -0.5 and 0.1 V/Å, the electronic gap decreases lineary with the increase of the electric field. In the third region, where E_{ext} is between 0.1 and 0.8 V/Å, the heterostructure In_2Se_3/Bi_2Se_3 shows a transition from a semiconductor to a metal. However, when the intrinsic dipole of In_2Se_3 is in the opposite direction (the G_2 configuration), the observed behavior is different: when a negative electric field is applied, the band gap exhibits a linear increase. Then, when a positive electric field is applied, the variation of the electronic gap under the application of an external electric field is divided into two regions: when E_{ext} is between 0 and 0.2 V/Å, the value of the gap tends to stabilize as the electric field strength is increased, and when E_{ext} is between 0.4 and 0.8 V/Å, E_g exhibits a linear decreasing behavior as the electric field strength is increased. Finally, the non-ferrelectric configuration G_3 shows a metallic phase when E_{ext} is between -0.8 and -0.5 V/Å. Then, when the external electric field is betwen -0.5 and 0.6 V/Å, the band gap increases with E_{ext}, and when E_{ext} is between 0.6 and 0.8 V/Å, the gap value tends to stabilize as the electric field strength is increased.

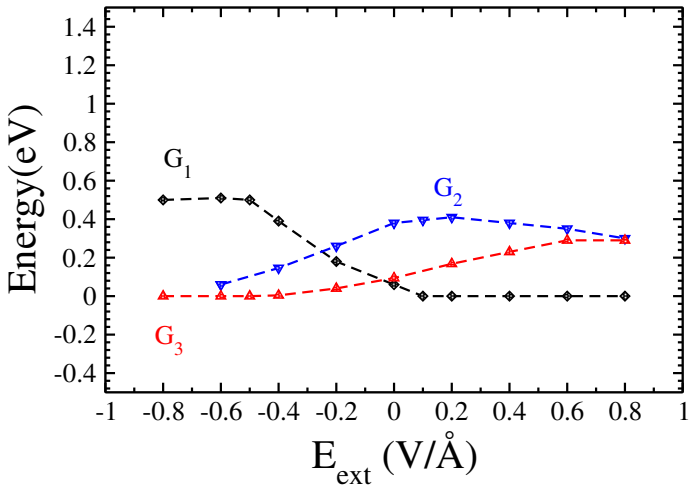

FIG. 5: Evolution of the band gap of the G_1, G_2 and G_3 configurations of the In_2Se_3/Bi_2Se_3 heterostructure as a function of strength of the external electric field (E_{ext}).

To better understand the effect of the external electric field on the electronic structure

of the heterostructure In_2Se_3/Bi_2Se_3, the edges of the valence bands (E_v) and conduction bands (E_c) of Bi_2Se_3 and In_2Se_3 are shown in figure 6. Interestingly, it is found that the In_2Se_3/Bi_2Se_3 heterostructure band alignment is changed from type II to type I under the application of the external electric field. We see in Figure 6(a) that the G_1 configuration shows a type II band alignment when E_{ext} is between -0.4 and 0.1 V/Å. Then, a crossing between the valence band maximums of In_2Se_3 and Bi_2Se_3 takes place for E_{ext} = -0,4 V/Å, indicating the transition from type II to type I. In this case, the VBM and CBM are dominated by the orbitals of the Bi_2Se_3 layer. Concerning the G2 configuration, we see in figure 6(b) that the external electric field does not change the origin of the VBM where its states come mainly from the orbitals of the Bi_2Se_3 layer. In contrast, the states of the CBM are dependent on the electric field. When the electric field is between -0.6 and 0.7 V/Å, the CBM states are dominated by the orbitals of the In_2Se_3 layer which leads to the formation of a type II band alignment. When the electric field is between 0.7 and 0.8 V/Å, the CBM states tend to be localized on the Bi_2Se_3 layer which makes the band alignment to become type I. The crossing between $E_{c(In)}$ and $E_{c(Bi)}$, which corresponds to a transition from a type II to a type I band alignment, takes place for E_{ext} = 0.7 V/Å. For the G3 configuration, we see in figure 6(c) that the VBM states belong to the Bi_2Se_3 layer, with and without the application of E_{ext}. On the other hand, the origin of the CBM states changes according to the external electric field. When E_{ext} is between -0.4 and 0.7 V/Å, the CBM states are dominated by the orbitals of In_2Se_3 layer, which leads to the formation of a type II band alignment. When E_{ext} is between 0.7 and 0.8 V/Å, the CBM is changed and is contributed by Bi_2Se_3, which leads to the formation of a type I band alignment.

Among the most important properties that determine the performance of heterostructure devices are the band offsets. These are the discontinuities between the valence band maximum VBM or conduction band minimum CBM of each semiconductor at their common interface which act as barriers to electrical transport through the interface. Therefore the difference in energy between the values of the conduction band minimum (the values of the valence band maximum) of In_2Se_3 and Bi_2Se_3 in In_2Se_3/Bi_2Se_3 heterostructure is defined as the conduction band offset $\Delta E_c = E_{c(In)} - E_{c(Bi)}$ (the valence band offset $\Delta E_v = E_{v(In)} - E_{v(Bi)}$), where $E_{c(In(Bi))}$ and $E_{v(In(Bi))}$ are the CBM and the VBM of In_2Se_3 (Bi_2Se_3) in the heterostructure In_2Se_3/Bi_2Se_3. Obviously, the conduction band and valence band offset values are dependent on the direction of the polarization of In_2Se_3 as shown in figure 3 : for the

G_1 configuration, where the intrinsic dipole is directed towards Bi_2Se_3, the conduction band and valence band offset values are 0.99 and 0.43 eV, respectively. For the G_2 configuration, when the ferroelectric polarization of In_2Se_3 is reversed, the conduction band and valence band offset values are 0.14 and 0.49 eV, respectively. For the non ferroelectric configuration G_3, the conduction band and valence band offset values are 0.34 and 0.47 eV, respectively. Under the application of an external electric field, the band offsets ΔE_c and ΔE_v of the different configurations (G_1, G_2 and G_3) present a linear increase with the increase of the external field, as presented in figure 6. The large values of $|\Delta E_c|$ and $|\Delta E_v|$ under electric field (positive or negative), when the configurations exhibit a type II band alignment, lead to a more efficient electron-hole separation and therefore an increase of the corresponding lifetime of the excitons, which can be very useful for certain optoelectronic applications.

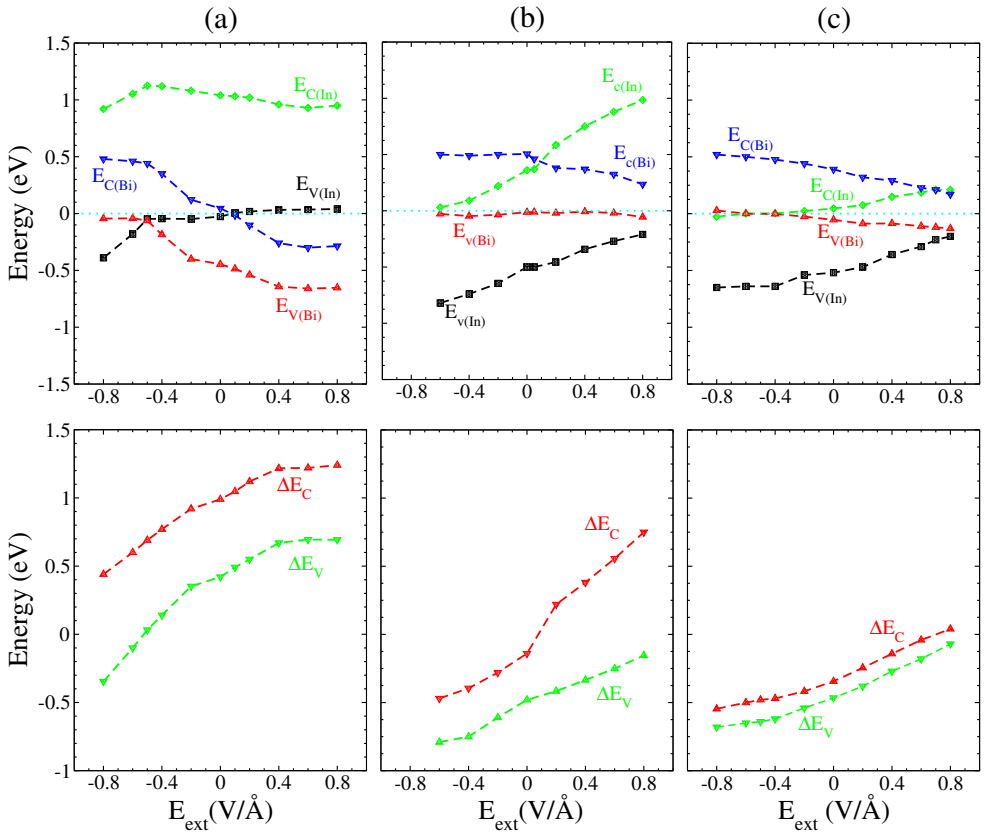

FIG. 6: (top panel) Evolution of the band edges of In_2Se_3 and Bi_2Se_3 and (bottom panel) evolution of the band offsets of (a) G_1, (b) G_2 and (c)G_3 configurations of the heterostructure In_2Se_3/Bi_2Se_3 as a function of the external field. $E_{c(In(Bi))}$ and $E_{v(In(Bi))}$ are the CBM and the VBM of In_2Se_3 (Bi_2Se_3) in In_2Se_3/Bi_2Se_3 heterostructure.

IV. CONCLUSION

In summary, the electronic properties of In_2Se_3/Bi_2Se_3 heterostructure have been investigated using density functional theory and the GW approximation. We have found that the In_2Se_3/Bi_2Se_3 ferroelectric heterostructure is a semiconductor with a direct bandgap. However, when the intrinsic polarization of In_2Se_3 is reversed, we have found that In_2Se_3/Bi_2Se_3 is a semiconductor with an indirect bandgap. By analysing the electron density, we found that the In_2Se_3/Bi_2Se_3 heterobilayer can be potentially used as an electron-hole charge separator. Our results show also that the In_2Se_3/Bi_2Se_3 heterostructure exhibits a modulation of its band gap and band offsets upon the variation of an external electric field. Also the In_2Se_3/Bi_2Se_3 heterostructure has a type II band alignment but under the application of an external electric field, it experiences a transition from type II to type I band alignment. Overall, the findings obtained in this study provide interesting guidelines for using the In_2Se_3/Bi_2Se_3 system in some electronic or optical devices, and open the path for further experimental and theoretical studies of this system.

[1] A. H. Castro Neto, F. Guinea, N. M. R. Peres, K. S. Novoselov, A. K. Geim, The electronic properties of graphene, Rev. Mod. Phys. 81 (2009) 109. doi:https://doi.org/10.1103/RevModPhys.81.109.

[2] K. S. Novoselov, A. K. Geim, S. V. Morozov, D. Jiang, Y. Zhang, S. V. Dubonos, I. V. Grigorieva, A. A. Firsov, Electric field effect in atomically thin carbon films 306 (2004) 666. doi:https://doi.org/10.1126/science.1102896.

[3] L. Debbichi, O. Eriksson, S. Lebègue, Two-Dimensional Indium Selenides Compounds: An Ab Initio Study, The Journal of Physical Chemistry Letters 6 (2015) 3098. doi:https://doi.org/10.1021/acs.jpclett.5b01356.

[4] D. Geng, H. Y. Yang, Recent Advances in Growth of Novel 2D Materials: Beyond Graphene and Transition Metal Dichalcogenides, Advanced Materials 30 (2018) 1800865. doi:https://doi.org/10.1002/adma.201800865.

[5] R. Kavitha, P. Nithya, S. Girish Kumar, Noble metal deposited graphitic carbon nitride based heterojunction photocatalysts, Applied Surface Science 508 (2020) 145142. doi:https://doi.org/10.1016/j.apsusc.2019.145142.

[6] Z. Zhibin, L. Chang, D. Zhimin, D. Ying, X. Guoxuan, L. Yuhui, W. Youqun, W. Yingcai, L. Yunhai, Synthesis of flower-like MoS2/g-C3N4 nanosheet heterojunctions with enhanced photocatalytic reduction activity of uranium(VI), Applied Surface Science 520 (2020) 146352. doi:https://doi.org/10.1016/j.apsusc.2020.146352.

[7] K. Khan, A. K. Tareen, M. Aslam, R. Wang, Y. Zhang, A. Mahmood, Z. Ouyang, H. Zhang, Z. Guo, Recent developments in emerging two-dimensional materials and their applications, J. Mater. Chem. C 8 (2020) 387. doi:https://doi.org/10.1039/C9TC04187G.

[8] M. Wu, P. Jena, The rise of two-dimensional van der Waals ferroelectrics, WIREs Computational Molecular Science 8 (2018) e1365. doi:https://doi.org/10.1002/wcms.1365.

[9] C. Cui, F. Xue, W. Hu, L. Li, Two-dimensional materials with piezoelectric and ferroelectric functionalities, npj 2D Materials and Applications 2 (2018) 18. doi:https://doi.org/10.1038/s41699-018-0063-5.

[10] W. Dimuthu, T. Cheng, Z. Chunmei, Z. Lei, M. Xin, D. Aijun, Bandstructure engineering in 2D materials using Ferroelectric materials, Applied Surface Science 513 (2020) 145817.

doi:https://doi.org/10.1016/j.apsusc.2020.145817.

[11] J. F. Scott, Ferroelectric memories today, Ferroelectrics 236 (2000) 247. doi:https://doi.org/10.1080/00150190008016056.

[12] M. Stengel, N. A. Spaldin, Origin of the dielectric dead layer in nanoscale capacitors, Nature 443 (2006) 679. doi:https://doi.org/10.1038/nature05148.

[13] E. F. Crawley, J. De luis, Use of piezoelectric actuators as elements of intelligent structures, AIAA Journal 25 (1987) 1373. doi:https://doi.org/10.2514/3.9792.

[14] X. Wang, J. Zhou, J. Song, J. Liu, N. Xu, Z. L. Wang, Piezoelectric Field Effect Transistor and Nanoforce Sensor Based on a Single ZnO Nanowire, Nano Letters 6 (2006) 2768. doi:https://doi.org/10.1021/nl061802g.

[15] H. Wang, F. Liu, W. Fu, Z. Fang, W. Zhou, Z. Liu, Two-dimensional heterostructures: fabrication, characterization, and application, Nanoscale 6 (2014) 12250. doi:https://doi.org/10.1039/C4NR03435J.

[16] K. S. Novoselov, A. Mishchenko, A. Carvalho, A. H. Castro Neto, 2D materials and van der Waals heterostructures, Science 353 (2016) aac9439. doi:https://doi.org/10.1126/science.aac9439.

[17] W. Zhang, C.-P. Chuu, al, Ultrahigh-gain Photodetectors Based on Atomically Thin Graphene-MoS2 Heterostructures, Scientific Reports 4 (2014) 3826. doi:https://doi.org/10.1038/srep03826.

[18] K. T. Butler, J. M. Frost, A. Walsh, Ferroelectric materials for solar energy conversion: photoferroics revisited, Energy Environ. Sci. 8 (2015) 838. doi:https://doi.org/10.1039/C4EE03523B.

[19] I. Grinberg, D. V. West, M. Torres, G. Gou, D. M. Stein, L. Wu, G. Chen, E. M. Gallo, A. R. Akbashev, P. K. Davies, J. E. Spanier, A. M. Rappe, Perovskite oxides for visible-light-absorbing ferroelectric and photovoltaic materials, Nature 503 (2013) 509. doi:https://doi.org/10.1038/nature12622.

[20] M. R. Morris, S. R. Pendlebury, J. Hong, S. Dunn, J. R. Durrant, Effect of internal electric fields on charge carrier dynamics in a ferroelectric material for solar energy conversion, Advanced Materials 28 (2016) 7123. doi:https://doi.org/10.1002/adma.201601238.

[21] Y. Zhou, D. Wu, Y. Zhu, Y. Cho, Q. He, X. Yang, K. Herrera, Z. Chu, Y. Han, M. C. Downer, H. Peng, K. Lai, Out-of-plane piezoelectricity and ferroelectricity in layered -In2Se3

nanoflakes, Nano Letters 17 (2017) 5508. doi:https://doi.org/10.1021/acs.nanolett.7b02198.

[22] C. Cui, W.-J. Hu, X. Yan, C. Addiego, W. Gao, Y. Wang, Z. Wang, L. Li, Y. Cheng, P. Li, X. Zhang, H. N. Alshareef, T. Wu, W. Zhu, X. Pan, L.-J. Li, Intercorrelated in-plane and out-of-plane ferroelectricity in ultrathin two-dimensional layered semiconductor In2Se3, Nano Lett. 18 (2018) 1253. doi:https://doi.org/10.1021/acs.nanolett.7b04852.

[23] W. Ding, J. Zhu, Z. Wang, Y. Gao, D. Xiao, Y. Gu, Z. Zhang, W. Zhu, Prediction of intrinsic two-dimensional ferroelectrics in In2Se3 and other III2-VI3 van der Waals materials, Nature Communications 8 (2017) 14956. doi:https://doi.org/10.1038/ncomms14956.

[24] Z. Shumin, X. Difa, C. Xiaohua, Z. Shiying, A. Changsheng, Construction of ultrathin 2D/2D g-C3N4/In2Se3 heterojunctions with high-speed charge transfer nanochannels for promoting photocatalytic hydrogen production, Applied Surface Science 528 (2020) 146858. doi:https://doi.org/10.1016/j.apsusc.2020.146858.

[25] Z. Guan, H. Hu, X. Shen, P. Xiang, N. Zhong, J. Chu, C. Duan, Recent Progress in Two-Dimensional Ferroelectric Materials, Advanced Electronic Materials 6 1900818. doi:https://doi.org/10.1002/aelm.201900818.

[26] T. Ayadi, L. Debbichi, M. Badawi, M. Said, H. Kim, D. Rocca, S. Lebègue, An ab initio study of the ferroelectric In2Se3/graphene heterostructure, Physica E: Low-dimensional Systems and Nanostructures 114 (2019) 113582. doi:https://doi.org/10.1016/j.physe.2019.113582.

[27] B. Liu, B. Tang, F. Lv, Y. Zeng, J. Liao, S. Wang, Q. Chen, Photodetector based on heterostructure of two-dimensional WSe2/In2Se3, Nanotechnology 31 (2019) 065203. doi:https://doi.org/10.1088/1361-6528/ab519b.

[28] X.-L. Qi, S.-C. Zhang, Topological insulators and superconductors, Rev. Mod. Phys. 83 (2011) 1057. doi:https://doi.org/10.1103/RevModPhys.83.1057.

[29] B. Fauqué, N. P. Butch, P. Syers, J. Paglione, S. Wiedmann, A. Collaudin, B. Grena, U. Zeitler, K. Behnia, Magnetothermoelectric properties of Bi_2Se_3, Phys. Rev. B 87 (2013) 035133. doi:https://doi.org/10.1103/PhysRevB.87.035133.

[30] G. Donglin, H. Chenguo, Ultrahigh thermoelectricity of atomically thick Bi2Se3 single layers: A computational study, Applied Surface Science 321 (2014) 525. doi:https://doi.org/10.1016/j.apsusc.2014.09.191.

[31] K. Seungyeon, L. Sangsoo, W. Jeongseok, L. Geunseop, Growth of Bi2Se3 topological insulator thin film on Ge(111) substrate, Applied Surface Science 432 (2018) 152. doi:https://doi.org/10.1016/j.apsusc.2017.03.029.

[32] Z. Hongbin, S. Zelong, L. Dong, X. Yancai, L. Jian, B. Chengjie, M. Baoyuan, Near-infrared photodetection based on topological insulator P-N heterojunction of SnTe/Bi2Se3, Applied Surface Science 509 (2020) 145290. doi:https://doi.org/10.1016/j.apsusc.2020.145290.

[33] Z. Li-Bo, Y. Chuan-Lu, W. Mei-Shan, M. Xiao-Guang, Two-dimensional Bi2Se3 monolayer with high mobility and enhanced optical absorption in the UVvisible light region, Physica E: Low-dimensional Systems and Nanostructures 124 (2020) 114272. doi:https://doi.org/10.1016/j.physe.2020.114272.

[34] S. J. Rathi, D. J. Smith, J. Drucker, Optimization of In2Se3/si(111) heteroepitaxy to enable Bi2Se3/In2Se3 bilayer growth, Crystal Growth and Design 14 (2014) 4617. doi:https://doi.org/10.1021/cg500722n.

[35] G. Kresse, J. Hafner, *Ab initio* molecular dynamics for liquid metals, Phys. Rev. B 47 (1993) 558. doi:https://doi.org/10.1103/PhysRevB.47.558.

[36] G. Kresse, D. Joubert, From ultrasoft pseudopotentials to the projector augmented-wave method, Phys. Rev. B 59 (1999) 1758. doi:https://doi.org/10.1103/PhysRevB.59.1758.

[37] J. P. Perdew, K. Burke, M. Ernzerhof, Generalized Gradient Approximation Made Simple, Phys. Rev. Lett. 77 (1996) 3865. doi:https://doi.org/10.1103/PhysRevLett.77.3865.

[38] A. Tkatchenko, M. Scheffler, Accurate Molecular Van Der Waals Interactions from Ground-State Electron Density and Free-Atom Reference Data, Phys. Rev. Lett. 102 (2009) 073005. doi:https://doi.org/10.1103/PhysRevLett.102.073005.

[39] F. L. Hirshfeld, Bonded-atom fragments for describing molecular charge densities, Theoretica chimica acta 44 (1977) 129. doi:https://doi.org/10.1007/BF00549096.

[40] T. Bučko, S. Lebègue, J. G. Ángyán, J. Hafner, Extending the applicability of the Tkatchenko-Scheffler dispersion correction via iterative Hirshfeld partitioning, J. Chem. Phys. 141 (2014) 034114. doi:http://dx.doi.org/10.1063/1.4890003.

[41] T. Bučko, S. Lebègue, J. Hafner, J. G. Ángyán, Improved Density Dependent Correction for the Description of London Dispersion Forces, J. Chem. Theory Comput. 9 (2013) 4293. doi:https://doi.org/10.1021/ct400694h.

[42] F. Aryasetiawan, O. Gunnarsson, The GW method, Reports on Progress in Physics 61 237. doi:https://doi.org/10.1088/0034-4885/61/3/002.

[43] Properties of electron self-energies and their role in electron spectroscopies, Nuclear Instruments and Methods in Physics Research Section A: Accelerators, Spectrometers, Detectors and Associated Equipment 308 (1991) 169. doi:https://doi.org/10.1016/0168-9002(91)90619-2.

[44] T. Ayadi, L. Debbichi, M. Said, S. Lebègue, An ab initio study of the electronic structure of indium and gallium chalcogenide bilayers, J. Chem. Phys. 147 (2017) 114701. doi:https://doi.org/10.1063/1.4997233.

[45] L. Debbichi, O. Eriksson, S. Lebègue, Electronic structure of two-dimensional transition metal dichalcogenide bilayers from ab initio theory, Phys. Rev. B 89 (2014) 205311. doi:https://doi.org/10.1103/PhysRevB.89.205311.

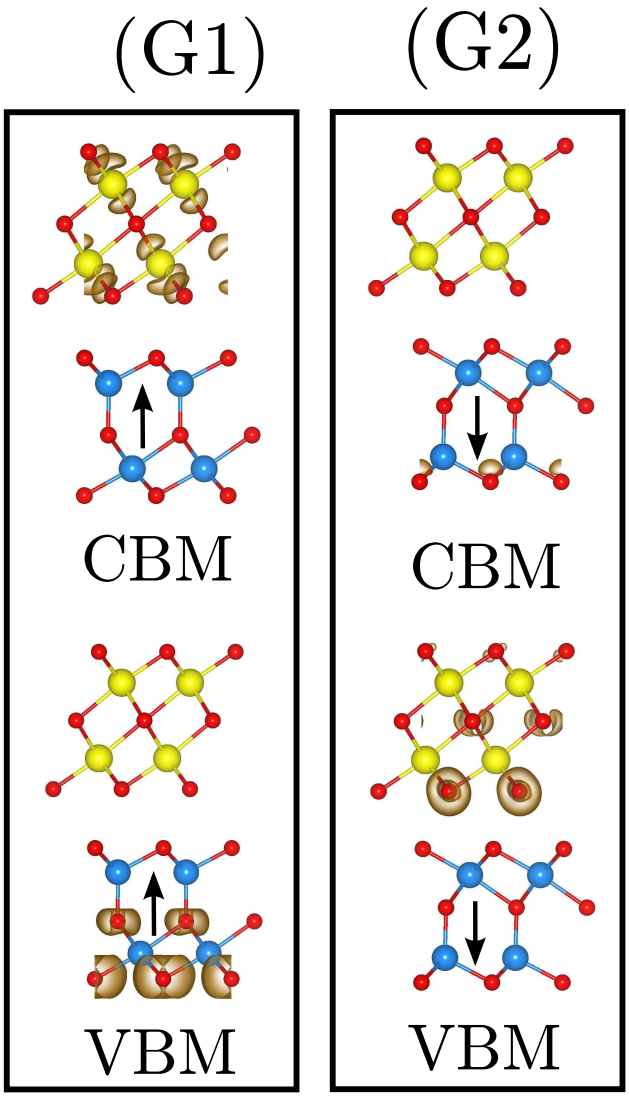
(G1)
(G2)
CBM
CBM
VBM
VBM